



Separated Flow Response to Rapid Flap Deflection

Albert Medina*

U.S. Air Force Research Laboratory, Wright-Patterson Air Force Base, Ohio 45433

Maziar S. Hemati†

University of Minnesota, Minneapolis, Minnesota 55455

and

Matthew Rockwood‡

U.S. Air Force Research Laboratory, Wright-Patterson Air Force Base, Ohio 45433

<https://doi.org/10.2514/1.J058367>

The transient response of a massively separated flow over an airfoil to rapid flap actuation is presented. A NACA 0006 airfoil is oriented at a fixed incidence of 20 deg for a Reynolds number of $Re = 4 \times 10^4$. The experiments are performed in a water tunnel with a wing spanning the width of the test section to produce a nominally two-dimensional flowfield. The airfoil is bisected about the midchord position, resulting in a 50%-chord trailing-edge flap. The flap is rapidly deflected in a smoothed-ramp profile over a range of deflection speeds and amplitudes. The flap maneuver is completed in a fraction of a single convective time. Focus is given to a deflection amplitude of 2 deg to minimize geometric deviation from the nondeflected configuration. The desired response to such a flap motion is the evocation of vortical transients conducive to lift enhancement. Through this study, two distinct transient responses are observed that are directionally dependent on flap actuation. In motions resulting in an increase in airfoil camber, the lift is increased instantaneously to modest values before relaxation to a separated steady state. In effect, this mode expedites convergence to the steady-state value of the final airfoil configuration and is devoid of the “antlift” spike associated with the discrete actuation of conventional fluidic actuators. In motions resulting in a decrease in airfoil camber, the lift profile is characterized by an initial reduction before a surge in lift, culminating in a global peak and followed by relaxation. Both deflection modes prove disruptive to the leading-edge shear-layer dynamics through trailing-edge actuation and are cause for rollup of a leading-edge vortex. Ridges of the finite-time Lyapunov exponent field are used to determine that the net decrease in camber motion induces significant entrainment near the trailing edge, leading to a smaller recirculation region and reattachment of the flow above the suction surface trailing-edge region. The net increase in camber motion does not generate this entrainment, and therefore yields a significantly larger recirculation region.

Nomenclature

a	=	smoothing coefficient
$a_n(t)$	=	n th temporal coefficient
b	=	wing span
CD	=	drag coefficient
CL	=	lift coefficient
c	=	airfoil chord
D	=	drag
k	=	nondimensional flap deflection rate
L	=	lift
Q_{\max}	=	global maximum Q value
Re	=	Reynolds number
S	=	wing planform area
t	=	time
t_1	=	nonsmoothed-ramp deflection start time
t_2	=	nonsmoothed-ramp deflection end time
U	=	freestream velocity
u_i	=	i th component of velocity
x	=	streamwise coordinate
y	=	transverse coordinate

α_{LE}	=	fore-element angle of attack
Γ	=	circulation
$\delta(t)$	=	flap deflection angle
δ_A	=	flap deflection amplitude
δ_F	=	final flap angle
δ_M	=	mean flap deflection
δ_0	=	initial flap angle
$\dot{\delta}_{\max}$	=	maximum flap deflection speed
λ_n	=	n th mode eigenvalue
ρ	=	fluid density
σ	=	fitting parameter
ω	=	vorticity

I. Introduction

THE deleterious effects of flow separation in aerodynamics have long motivated pursuits toward active flow control with ambitions of mitigating performance degradation or expanding operational envelopes. Design objectives include lift enhancement, drag reduction, delayed onset of stall, and separation recovery for greater control-surface authority. To this end, there stands a need to develop a deeper understanding of the underlying phenomena associated with baseline separated flows and the receptivity of such flows to actuation and perturbation. Such fundamental knowledge is necessary to furnish full-scale control applications where, as Williams et al. [1] concluded, improved lift control in unsteady flows requires improved understanding and modeling of the flow response to actuation, modeling of the unsteady aerodynamics, and a controller capable of reacting to these effects. It is therefore essential to measure the dynamic response of separated flows to actuator input when seeking predictive capabilities for an effective active flow control system. At the rudimentary level, quantifying the flow response to actuation is complicated by the unsteady nature of flow separation that bears host to a number of instabilities. As Raju et al. [2] identified, these instabilities can be categorized as the Kelvin–Helmholtz instability

Presented as Paper 2018-0574 at the 2018 AIAA Aerospace Sciences Meeting, Kissimmee, FL, January 8–12, 2018; received 7 February 2019; revision received 29 August 2019; accepted for publication 16 January 2020; published online 27 February 2020. This material is declared a work of the U.S. Government and is not subject to copyright protection in the United States. All requests for copying and permission to reprint should be submitted to CCC at www.copyright.com; employ the eISSN 1533-385X to initiate your request. See also AIAA Rights and Permissions www.aiaa.org/randp.

*Research Scientist, Aerodynamic Technology Branch, Aerospace Vehicles Division, Aerospace Systems Directorate. Senior Member AIAA.

†Assistant Professor, Department of Aerospace Engineering and Mechanics. Senior Member AIAA.

‡Research Scientist, AS&M, Aerodynamic Technology Branch, Aerospace Vehicles Division, Aerospace Systems Directorate. Member AIAA.

within the leading-edge shear layer, the shedding instability of the leading-edge vortex, and the instability in the wake of the airfoil. The desired effect of actuation is then the suppression of instabilities near their respective sites of inception to mitigate propagation and amplification into the global flowfield.

The fundamental lift response resulting from impulselike actuator input has been a ubiquitous initial lift reversal spike followed shortly by a surge in lift incremented above the steady baseline performance before relaxation to an undisturbed state. Under single pulse actuation by a Lorentz force, Albrecht et al. [3] demonstrated insensitivity in the resultant lift transient profile to the actuation direction: be it oriented downstream or upstream. Although actuator direction proved influential on the initial development of the shear layer and the initiation of the reattachment process, the separation envelope bore the same response irrespective of pulse direction. Experiments by Brzozowski et al. [4] examined the receptivity of the separated flow above a stalled airfoil to a single short pulse ($t_{\text{pulse}}U/c = 0.04$) employing pulse-combustion actuators. Brzozowski et al. described two prominent effects observed within the separated flow dynamics in response to actuation: 1) the severance of the separated vorticity layer from the airfoil surface; and 2) ensuing advection of a large-scale clockwise vortex and the rollup of a corotating vorticity layer that advects along the airfoil surface. A momentary decrease in circulation was said to be attributed to the shedding of the severed clockwise vortex, and the formation and advection of the surface shear layer led to a net increase in circulation and lift. Through continuous actuation, several works have demonstrated the ability to sustain flow reattachment on the airfoil. However, as Amitay and Glezer determined [5,6], the transient response to step-change or impulselike actuator input could be used in transient actuator pulses to generate higher lift coefficients than could be obtained through continuous actuation. Similarly, Margalit et al. [7] found a short duty cycle to be of substantial influence on the normal force coefficient corresponding to a delta wing platform at a high incidence angle.

The aforementioned works are in concordance in their spatial selection of actuator placement favoring proximity to the leading edge. The anterior placement is localized near the separated shear layer in a targeted effort at favorably disrupting the baseline flow. The emphasis on placement is further reinforced in recognition of its crucial role in governing the effectiveness of a given actuator. Methods proposed by Natarajan et al. [8] and Chomaz [9] have provided frameworks to inform the placement of actuation sites by identification of spatial locations of maximum receptivity in the system. The effective locations of control are obtained by the overlap of forward and adjoint global modes of the system corresponding to regions of high dynamic sensitivity. However, with an objective of generating enhanced lift, the proper placement of an actuator may prove actuator specific. In instances of employing blowing control, simulations by Huang et al. [10] have highlighted the dependency of elevated lift on the chordwise location where greater lift was produced with actuation applied further downstream of the airfoil leading edge, peaking at $0.8c$ for tangential blowing. The resulting mechanism by which lift

was enhanced did not appear contingent on excitation of the leading-edge flowfield.

In the present study, a NACA 0006 airfoil is held at a fixed incidence of 20 deg presenting a prototypical massively separated state. The susceptibility of the deep-stalled airfoil to rapid low-amplitude steps in flap deflection is investigated. This work is distinguished from literature in its application of posterior mechanical actuation to incite leading-edge transient phenomena conducive to lift enhancement and flow reattachment. In the current measurements, a case is made for the receptivity of a massively separated flow to rapid flap maneuvers through examination of the lift response to ramp rate and through interrogation of the resultant flowfield evolution. The results highlight a means of flap actuation capable of producing favorable lift transients devoid of the classical “lift reversal” but instead generate an instantaneous incremented lift.

II. Experimental Setup

Experiments were performed in the U.S. Air Force Research Laboratory Horizontal Free-Surface Water Tunnel, presented in Fig. 1 (left). The tunnel has a 4:1 contraction and a 46-cm-wide by 61-cm-high test section with a free-surface speed range of 3–105 cm/s and a streamwise-component turbulence intensity of $\sim 0.4\%$ at 15–40 cm/s. The tunnel is fitted with a three-degree-of-freedom motion stage consisting of a triplet of H2W Technologies linear motors and driven by AMC DigiFlex servo drives interfaced with a Galil DMC 4040 four-axis motion controller with user-selected proportional–integral–derivative gain constants for each axis. A plastic three-dimensionally printed NACA 0006 airfoil of 200 mm chord (physical aspect ratio of 2.25) and strengthened by spanwise carbon-fiber rods is bisected about the midchord position as shown in Fig. 1 (right). The test article spans the test section with a nominal 1 mm gap at each wingtip to produce a nominally two-dimensional flowfield. The fore element of the airfoil is rigidly connected to the plunge rod of the front vertical linear motor. The aft element, or flap, is analogously connected to the rear vertical linear motor but is constrained by a linkage mechanism to the front motor plunge rod such that relative motion between the two vertical motors results in a pitching motion of the flap. The fore element is held at fixed incidence (which can be changed by swapping out its mounting arm), whereas the rear element is so displaced that its motion relative to the fore element enacts a pivot about the gap between the two airfoil elements. This gap measures 0.5 mm and is bridged with a flexible rubber film of 0.2 mm thickness to prevent flare up. The flap incidence angle is limited to ± 45 deg with respect to the horizontal plane. The fore-element fixed-incidence angle is $\alpha_{\text{LE}} = 20$ deg, corresponding to a prototypical separated flow [11].

A force measurement was conducted via two ATI NANO-25 IP68 six-component force balances. Each airfoil element was supplied a dedicated force balance affixed to its respective frame. More important, there is no mechanical connection between the fore and aft elements; the forces of each element were therefore measured independently. Measurements were sampled at a rate of 1 kHz and

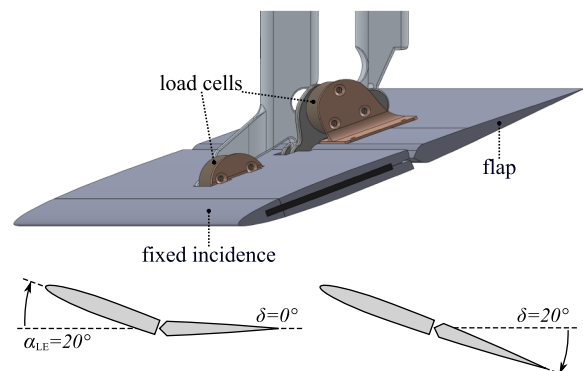
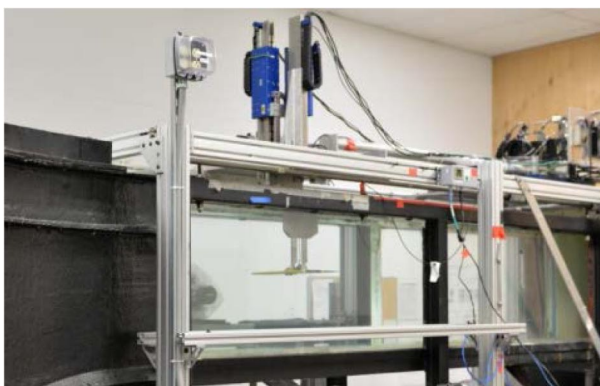


Fig. 1 (left) Water tunnel facility. (right) NACA 0006 configuration and angular definitions.

treated with a Butterworth low-pass filter of 10 Hz. Force histories were constructed from ensemble averaging over 10 consecutive runs. Static forces were derived from time averaging over a hold period of 10 s for each flap deflection angle. The lift coefficient was nondimensionalized as $C_L = (L/0.5\rho U^2 S)$, where L is the measured lift, ρ is the fluid density, U is the freestream velocity, S is the planform area, and c is the chord length. The maximum uncertainty in lift coefficient of the representative case ($\alpha_{LE} = 20$ deg, $\delta = 20$ deg \rightarrow 18 deg, and $0.16tU/c$ nominal flap-motion duration) was estimated to be less than 7.6% of the maximum coefficient of lift (Fig. 2). The uncertainty incorporates the repeatability of the force history among an ensemble of 10 experimental runs. Bias error sources include the model attitude, flap orientation, and flow quality. The repeatability or precision error was based on the standard deviation of the ensemble, and it corresponds to a 95% confidence interval, assuming a normal distribution (two standard deviations). Much of the uncertainty stems from fluctuations associated with the massively separated state of the test article. Confidence intervals are displayed for select cases (Figs. 2 and 3) as shaded regions about their respective color-coded means.

Planar flow visualization was performed at the three-quarter spanwise position. Rhodamine-590 was introduced at the leading edge and the trailing edge of the airfoil and fluoresced by illumination of a Nd:YLF laser sheet (Photonics Industries DM50-527, 55 mJ/pulse, 10 kHz maximum). To minimize surface reflections, the camera was outfitted with an optical filter (Tiffen, Orange 21) compatible with the fluorescence emission. Velocity field data were obtained by using

the same laser sheet setup to perform particle image velocimetry. The time-resolved particle image velocimetry (PIV) data are two-dimensional and two-component, and they are confined to the in-plane velocity field. For seeding, polyamide particles of 20 μm in diameter (LaVision, SG = 1.03) were introduced into the tunnel. Within the light sheet, the x and y components of velocity are calculated by the correlation of single-exposure double-frame image pairs using Fluere (Version 1.3). Image pairs were correlated using multipass, multigrid interrogation with window sizes of 64×64 to 48×48 with 50% overlap to produce a mean signal-to-noise ratio of 5.4. The resulting vector resolution was 76 vectors per total chord. The velocity fields presented in this work are the results of ensemble averaging over 10 consecutive experimental runs.

The flap motion is described by four parameters: initial flap angle δ_0 , final flap angle δ_F , frequency of motion f , and smoothing coefficient a . The kinematic schedule begins with a sinusoidal waveform $\delta(t) = \delta_M + \delta_A \cos(2\pi ft)$, where δ_M is the mean incidence angle ($(\delta_F + \delta_0)/2$), δ_A is the deflection amplitude $(\delta_0 - \delta_F)/2$, and f is the frequency in hertz. Then, a C^∞ -smoothing ramp function suggested by Ol et al. [12] is fitted to the sinusoidal waveform over a semiperiod, resulting in a motion given by Eq. (1):

$$\delta(t) = \frac{k}{a} \ln \left[\frac{\cosh(a(t-t_1)U/b)}{\cosh(a(t-t_2)U/b)} \right] + \frac{\delta_F + \delta_0}{2} \quad (1)$$

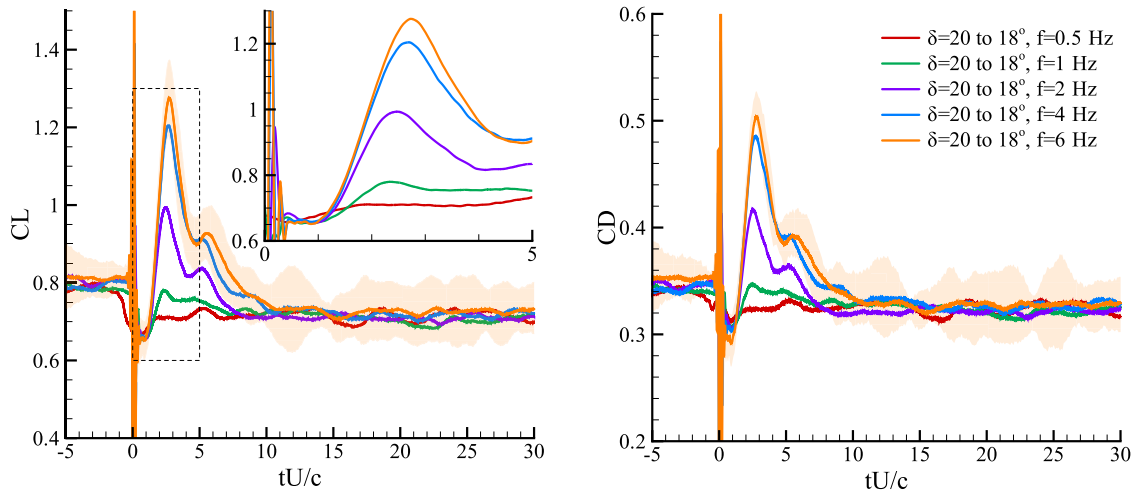


Fig. 2 Lift and drag coefficient response to flap ramp-rate: $\delta = [20 \text{ deg} - 18 \text{ deg}]$, $f_{\text{sine}} = [0.5, 1, 2, 4, 6]$ Hz. Motion commences at $tU/c = 0$.

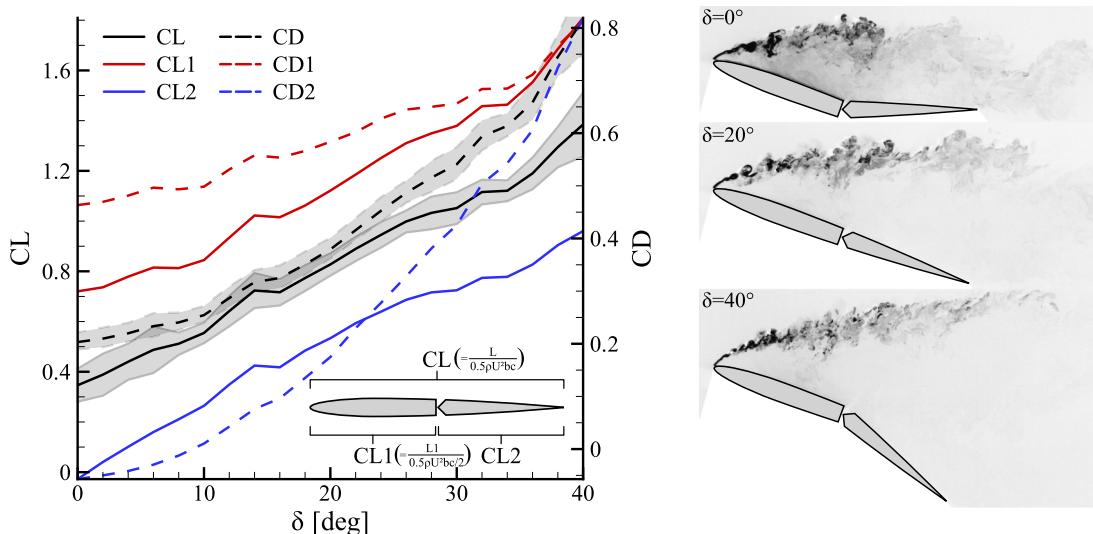


Fig. 3 Static lift and drag coefficient vs deflection angle $\delta = [0-40 \text{ deg}]$; the leading element is at fixed incidence $\alpha_{LE} = 20$ deg. Deflection angle $\delta = 20$ deg corresponds to a planar configuration.

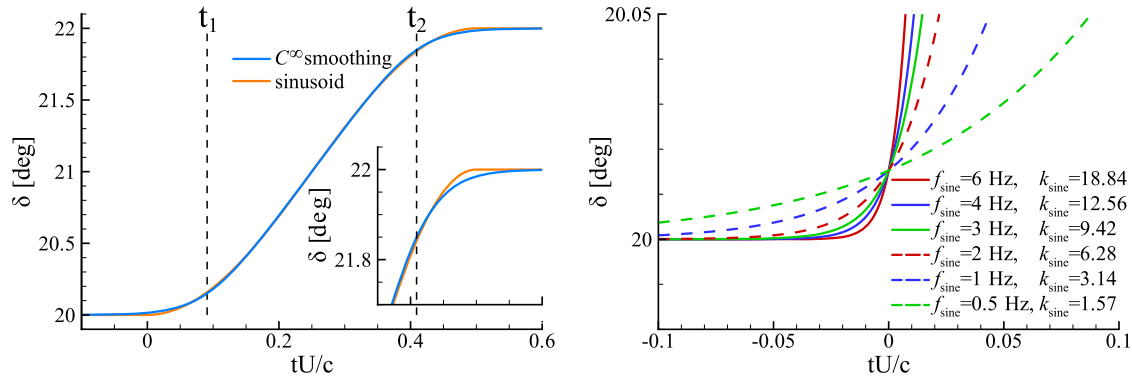


Fig. 4 Typical kinematic profile for flap deflection: (left) C^∞ -smoothing of a sinusoidal waveform (right) effects of smoothing on kinematic start time.

where $k = \dot{\delta}_{\max} b/2U$ is the nominal deflection rate; $a = \pi^2 k/(2|\delta_F - \delta_0|(1 - \sigma))$ is the smoothing parameter; σ is a fitting parameter proposed by Granlund et al. [13]; b is the semichord; and time constants t_1 and t_2 , respectively, correspond to the start and completion of flap motion for the nonsmoothed deflection profile. The duration of the nonsmoothed motion ($t_2 - t_1$) is derived by matching its ramp rate to the peak slope of the sinusoidal waveform. The resulting smoothed motion preserves the sine-wave peak velocity. Flap incidence angles are measured with respect to the horizontal plane, as illustrated in Fig. 1 (right).

The freestream speed is $U = 200$ mm/s that, with a 200 mm chord, gives a nominal chord-based Reynolds number of $Re \sim 40,000$ in water maintained at room temperature (~ 20 deg C). Conveniently, one convective time is also numerically 1 s of wall-clock time. Thus, for a frequency of 1 Hz, the flap motion completes approximately over a semiperiod of 0.5 s, or one-half of one convective time: $0.5tU/c$. The C^∞ smoothing slightly broadens the kinematic profile; a representative case is given in Fig. 4 (left). The effect of smoothing over a range of frequencies is presented with more rigor in Fig. 4 (right) where the original sinusoidal profile commences at $tU/c = 0$. The parametric space of interest is summarized in Table 1.

III. Results and Discussion

Direct force measurements and dye visualization were used to gauge the receptivity of a massively separated flow to rapid flap deflection. Here, the term “rapid” is reserved for flap deployments realized within one convective time. Employing a generously scaled flap as the choice of control method is distinct from conventional mechanisms (be they jets, plasma, blowing/suction, acoustic forcing, or Lorentz forces) in that the flap is coupled with the airfoil geometry and the resulting aerodynamic signature. Any motions performed by the flap ultimately modify the lift capabilities of the airfoil by virtue of inciting transients in addition to the reconfiguration of the lifting surface. Nevertheless, flap actuation still abides by many of the parameters of its more modern counterparts: excitation amplitude (deflection amplitude), excitation width (duration of deflection or deflection rate), and direction (net increase or decrease in camber). The greatest constraint of the proposed control method is

the mechanical limitations of deflection amplitude, and perhaps the deflection rates required of excitation. Moreover, because the intention of rapid flap deflection is to reconcile the baseline separated state of the airfoil with a state of elevated lift performance, consideration is given to deflection amplitudes conducive to the nominal preservation of the planar airfoil configuration. Therefore, focus is primarily given to a deflection step of $|\Delta\delta| = 2$ deg ($= |\delta_F - \delta_0|$), which presents minimal deviation from the initially nondeflected configuration and amounts to a change in effective attack angle of $\Delta\alpha_{\text{eff}} = 1$ deg (as observed in baseline attached flow measurements [14]). Before examining the transient aerodynamic response, the static effects of flap deflection on a baseline separated flow ($\alpha_{\text{LE}} = 20$ deg) are described.

A. Baseline Performance: Static Survey

The results for static lift and drag coefficient in response to flap deflection are shown in Fig. 3 (left). Total lift production exceeds drag for all deflection angles considered: $\delta = [0-40$ deg]. The resulting lift slope is roughly constant with total C_L bearing an approximate linear dependence on flap deflection. The total drag coefficient C_D appears to adhere to a parabolic profile, increasing with the deflection angle. The modular construction of the test article also grants force measurements of the individual fore [separated leading edge (LE)] and aft (flap) elements, as demonstrated in Fig. 1. For the individual elements, the semichord length was selected for normalization of the force coefficients, whereas the total chord length was used for the total force coefficients. The semichord length corresponds to the fore- and aft-element lengths as the airfoil is bisected about the midchord. The individual lift coefficients demonstrate a nonlinear deflection-angle dependency, particularly for $\delta > 20$ deg; whereas trends further diverge from lift trajectories set at $\delta < 20$ deg. The drag coefficients of the two elements resume the profile observed in C_D . Drag on the fore element exceeds that of the flap for all deflection angles until $\delta = 40$ deg where the two profiles are unified. In its most streamlined configuration, the flap is oriented parallel to the freestream at $\delta = 0$ deg, where it is in essence shielded by the leading element and offers little impedance to the freestream flow. This configuration translates to negligible lift and drag production by the flap. The accompanying qualitative imaging presented in Fig. 3 (right) is suggestive of the juxtaposition of the organization of separated structures with respect to trends in the aerodynamic forces. All flow snapshots evince considerable separation, evidenced by the shear layer emanating from the leading edge and no discernible reattachment to the airfoil further downstream. The shear layer appears subject to a Kelvin–Helmholtz instability, which transitions into regions of enhanced mixing that are convected downstream. The relative trajectory of the shear layer diverges further upward from the leading edge with increasing deflection angle. The influence of trailing-edge formations on inducing a downward momentum on the shear layer are diminished with net increases in camber. Accordingly, greater deflection amounts to an increase of the recirculating region aboard the suction surface of the airfoil where speeds are reduced below that of the freestream.

Table 1 Motion parameters

$ \Delta\delta $	f_{sine} , Hz	k_{sine}	$ \dot{\delta} _{\max} c/U$, deg
2 deg	0.5	1.5708	3.1416
	1	3.1416	6.2832
	2	6.2832	12.5664
	4	12.5664	25.1327
	6	18.8496	37.6991
1 deg	0.5	1.5708	1.5708
	1	3.1416	3.1416
	2	6.2832	6.2832
	4	12.5664	12.5664
	6	18.8496	18.8496

B. Transient Response to Rapid Flap Deflection

The effect of a single low-amplitude ramp motion by the flap on the transient lift response of the separated airfoil was studied by direct force measurement. The leading element was held fixed at 20 deg incidence, and the flap concluded its motion at $\Delta\delta = \pm 2$ deg from its initial angle of $\delta_0 = 20$ deg. As previously noted, the deflection amplitude is intended to provide a minimal excursion from the initial planar airfoil configuration ($\alpha_{LE} = \delta_0 = 20$ deg). The effects of a flap ramp rate on lift and drag for $\Delta\delta = -2$ deg (negative final camber) are shown in Fig. 2. Regardless of ramp rate, it should be understood that the lift and drag coefficients ultimately return to their respective asymptotic static values (Fig. 3) corresponding to the final flap angle. The contribution of noncirculatory force to lift and drag is constrained to a brief window coinciding with the duration of flap motion and is represented by the initial impulsive spikes tracking with the flap acceleration initiated at $tU/c = 0$ and terminating shortly thereafter. Barring the inertial or noncirculatory spikes associated with the acceleration phases of the flap, the ramp motion is cause for a transient spike in lift and drag exceeding steady-state values. The dynamic lift profile that follows from the actuation period bears the hallmarks of the lift response observed in conventional control schemes [1]: immediately after actuation, there exists a reduction in lift to a global minimum before a steep surge culminating in a global maximum and then relaxation of lift to a static value. The decremented state of lift (with respects to the initial deflection-angle value) persists for approximately $\Delta tU/c = 1.6$ for ramp rates associated with $k \geq 6.28$ ($f \geq 2$ Hz). Within these speeds of operation, the lift peak converges to $tU/c = 2.7$ with increasing ramp rate. An inset image of lift coefficient highlights this convergence. The descent from peak lift is accentuated by a minor local peak nearing $tU/c = 5.4$ where lift production maintains a value in excess of the initial steady state.

Thus far, the distinction has been made for rates associated with $k \geq 6.28$ where the characteristic response profile is readily identifiable, albeit scaled in some proportion to ramp rate. However, uniform among all the ramp rates of Fig. 2 is the initial decremented lift and the duration in which transients persist before recovery of a final steady state approaching $tU/c = 10$. The latter would suggest the duration of transient behavior scales as convective time rather than ramp rate. In this light, the ramp rate is suspected to incite a suite of flow dynamics above the airfoil, and the extent of their influence on the aerodynamic performance of the airfoil is predicated on the rate by which the flow structures are convected downstream. As the ramp rate is increased from $k = 3.14$ ($f = 1$ Hz) to $k = 6.28$ (2 Hz), the final lift response profile is quickly adopted. Furthermore, the scaling of the transient peak spike with increasing ramp rate may be indicative of lift saturation near $f = 6$ Hz.

Reversing now the ramp direction to $\Delta\delta = +2$ deg (positive final camber), the aerodynamic response to flap deflection from $\delta = 20$ to 22 deg is made distinct from the $\Delta\delta = -2$ deg case by its positive

excitation time, transient profile, and lift increment. In contradistinction to the previous $\Delta\delta = -2$ deg case, the airfoil experiences an immediate positive step in lift (and drag) coefficient in tandem with flap excitation, as shown in Fig. 5. The step in lift surpasses the steady-state performance of $\delta = 22$ deg. This particular response mode is devoid of the deleterious negative lift spike characteristic of the conventional control mechanisms and demonstrates less variability among the transient responses corresponding to ramp rates of $k \leq 12.56$ ($f \leq 4$ Hz). The ensuing transient profile exhibits a primary and a secondary peak before relaxation to a steady state near $tU/c = 10$. In examination of Fig. 5, the disparity between peak lift production of the deflection rate $f = 6$ Hz and the remaining (lower) rates quickly becomes apparent with no immediately identifiable scaling guideline. The disparity is further highlighted by the inset image provided for lift coefficient. This is to suggest the peak ramp rate examined here satisfies some circulatory threshold necessary to induce a transient profile reminiscent of a response previously reserved for $\Delta\delta = -2$ deg. The realization of an instantaneous response is in agreement with previous works exploring larger excursions from a planar configuration in baseline attached and separated states [15]. As previously alluded, the duration of the force transients appears independent of flap direction, be it $\Delta\delta = -2$ deg or $+2$ deg. It is then apparent that the excitation of either of the two response modes is dependent on the direction of flap motion. Motions performed toward promoting a net increase in positive camber incite the immediate incremental response, and motions toward promoting a net decrease in positive camber generate a decremented lift state before realizing desired gains.

Lift measurements are repeated for $\Delta\delta = \pm 1$ deg in Fig. 6, which effectively reduces the maximum ramp rate of $\Delta\delta = \pm 2$ deg by half. The two response modes are preserved along with their directional-deflection dependency. The timing of the transient lift peaks is unaffected by the reduction in deflection amplitude. Although the primary lift peak among the two cases experiences a notable reduction for $\Delta\delta = \pm 1$ deg, the response of the secondary lift spike is much less discernible.

C. Flowfield Evolution for Rapid Flap Deflection

The vortical fields of Fig. 7 document the accompanying temporal evolution of separated structures in response to a negative-camber ramp ($\Delta\delta = -2$ deg) of $k = 18.85$ ($f = 6$ Hz) from an initial non-deflected configuration. Before flap motion, the flowfield is characterized by the pronounced shear layer billowing from the leading edge of the airfoil, as noted in the static survey. Shortly after motion completes, the leading-edge shear layer is disrupted by the incipient rollup at $tU/c = 0.25$. This is cause for a distinct gap to form within the leading-edge shear layer where a void now separates the rollup from the free-shear layer. This disruption continues to appreciate in circulatory strength at $tU/c = 0.5$ to form a discrete leading-edge vortex. Note that this instance in time is also coincident with the

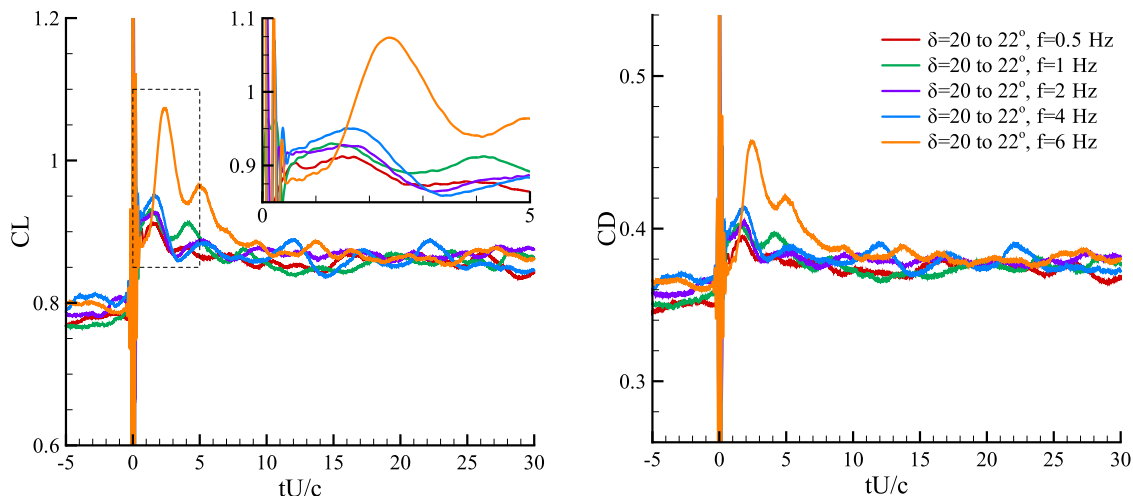


Fig. 5 Lift and drag coefficient response to flap ramp-rate: $\delta = [20 \text{ deg} - 22 \text{ deg}]$, $f_{\text{sine}} = [0.5, 1, 2, 4, 6]$ Hz. Motion commences at $tU/c = 0$.

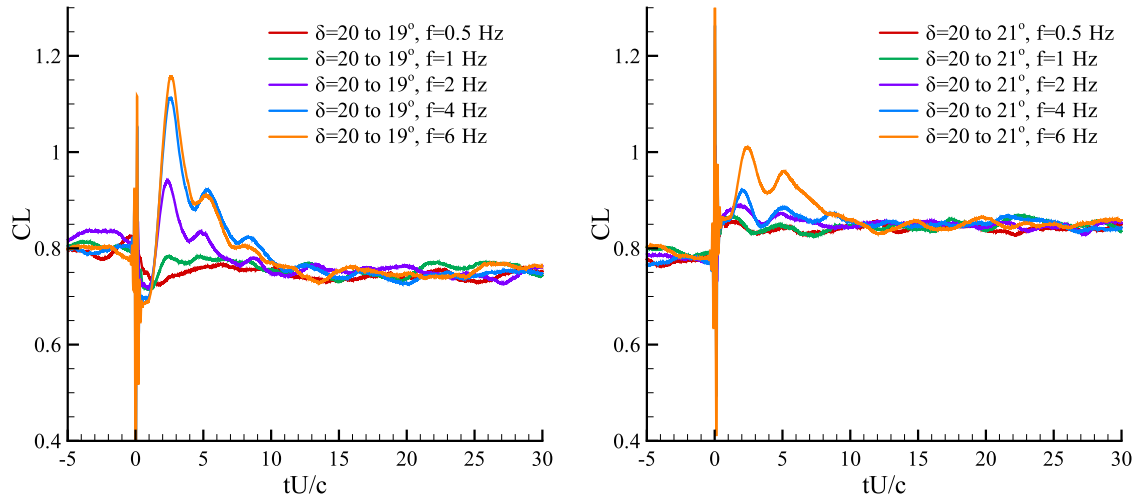


Fig. 6 Lift coefficient response to flap ramp-rate: (left) $\delta = [20 \text{ deg} -19 \text{ deg}]$ (right) $\delta = [20 \text{ deg} -21 \text{ deg}]$, $f_{\text{ sine}} = [0.5, 1, 2, 4, 6] \text{ Hz}$. Motion commences at $tU/c = 0$.

minimum lift generation observed in Fig. 2. Concurrently, there exists rollup about the airfoil trailing edge resulting in an oppositely signed trailing-edge vortex that is shed as a stopping vortex from the flap. The trailing-edge vortex is of comparable size to the nascent leading-edge formation. By $tU/c = 1.0$, lift still remains near the minimum value; and both the leading-edge and trailing-edge vortices have grown about their respective edges, with the trailing-edge vortex now convected slightly out of frame. Their joint formation is cause for vertical expansion of the separated region as the previously disrupted shear-layer formations navigate about the trailing-edge vortex periphery. The proximity of the trailing-edge vortex is thought

to promote a dominant clockwise swirl of the greater separated region. This results in the negatively signed vorticity of the free-shear layer to form into a circular clockwise vortex located above the flap. At this time, the leading-edge vortex has appreciated in strength and begins to impose reattachment near the $0.3c$ chord position.

Further reattachment is realized at $tU/c = 1.57$ where the bulk of the separated region has convected to the trailing edge. The reattachment point has shifted further along the chord to approximately $0.5c$, and the resulting lift recovers to surpass the initial steady-state value of $\delta = 20 \text{ deg}$. As the leading-edge vortex continues to grow in size and strength at $tU/c = 2.0$, so too does the lift coefficient.

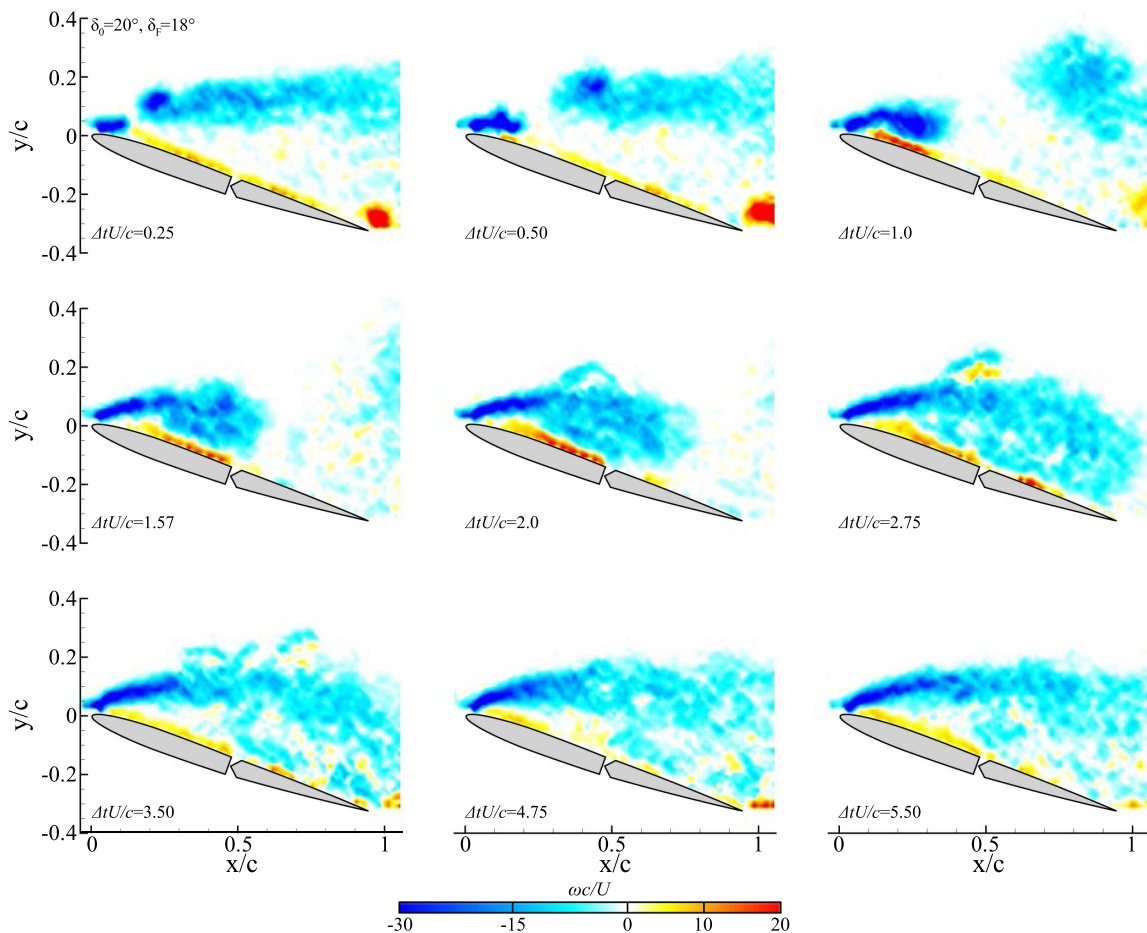


Fig. 7 Temporal evolution of vortical formations in response to a single rapid flap deflection ramp: $\Delta\delta = -2 \text{ deg}$ (net decrease in camber) at $f = 6 \text{ Hz}$.

The contour of the vortex adopts an elongated formation oriented nominally parallel to the airfoil surface. Peak lift production is achieved, approaching $tU/c = 2.75$ where reattachment now approaches the trailing edge. The leading-edge vortex appears as an arch with the resumption of a sporadic leading-edge shear layer. It is also noted that the eruption layer of counterclockwise vorticity beneath the leading-edge vortex has remained rather narrow during this process, resigned to a thin band adjacent to the airfoil surface. The descent in lift is coincident with the bulk of the initial leading-edge rollup traversing the chord and arriving at the trailing edge, as exemplified by $tU/c = 3.50$. The velocity induced at the trailing edge invites a layer of flow reversal that further removes the leading-edge vortex from the airfoil surface. Additionally, the eruption layer experiences expansion. The flowfield is returned to its nominal initial steady state by $tU/c = 5.5$. Although the flow field aboard the wing resumes its initial state the near-wake remains populated by transient formations now convected out of the plane of view.

The mechanisms by which the flap deflection schedule of $\Delta\delta = +2$ deg generates an instantaneous increase in lift remains a curious prospect. The vortical flowfield response to a positive-camber ramp is visualized in Fig. 8. Before deflection, both cases are unified in their baseline flowfields. The similarities depart as early as $tU/c = 0.25$ shortly after performing the ramp motion. Inspection of the leading-edge region reveals incipient rollup that, although disruptive to the shear layer, appears less distinguished from the overall standing shear layer. That is, the rollup region is still connected to the overarching free-shear layer. This would suggest the $\Delta\delta = +2$ deg ramp direction is conducive to a weaker disruption of the leading-edge shear layer. Nevertheless, the resulting flowfield produces an immediate incremented lift profile as demonstrated in Figs. 5 and 6. Disconnection of the free-shear layer from the leading-edge formation is visible at $tU/c = 0.5$. As the leading-edge vortex further matures at $tU/c = 1.0$, the differences in topology become

clearer. Just as before this phase of the flowfield is marked by the leading-edge vortex, inducing a downwash, and promoting reattachment and the ejection of the separated region from atop the airfoil. Notable differences from the $\Delta\delta = -2$ deg case include the lack of a counterclockwise trailing-edge vortex and the strained appearance of the leading-edge vortex. At $tU/c = 1.52$, the leading-edge vortex is dispersed over a slightly larger area than its negative-camber counterpart at $tU/c = 1.57$. Peak lift production at $tU/c = 2.38$ amounts to a diffused leading-edge vortex with a skew oriented along the airfoil surface. This instant is also coincident with the passage of the initial separated plume that has now convected downstream of the trailing edge. Once more, as lift descends during $tU/c = 3.10$, the trajectory of the overarching shear layer is further removed from the airfoil surface over the trailing edge. Lastly, the secondary lift peak generated at $tU/c = 5.0$ again highlights the importance of near-body wake dynamics in force production. The vortical field has nominally resumed its baseline separated state, yet transient lift is still generated by the dynamics just out of plain view.

As previously noted, a key distinction between the two deflection modes is the trailing-edge phenomena. For $\Delta\delta = -2$ deg, a prominent counterclockwise stopping vortex emanates from the trailing edge. Its evolution is depicted qualitatively through dye visualization in Fig. 9. Without the resolution concerns of quantitative analysis, the dye visualization presented here offers greater purview of the near-body wake with an expanded field of view. The trailing-edge vortex of $\Delta\delta = -2$ deg is effectively shielded from the freestream during these early stages of development. Its growth in size and downstream convection are documented within the sequence of images. At $tU/c = 1.57$, the trailing-edge vortex interacts with the ejected shear layer formation to produce a system of counter-rotating vortices. In the case of $\Delta\delta = +2$ deg, there remains little trace of the stopping vortex because its introduction at the trailing edge is subject to immediate interaction with the trailing-edge shear layer of

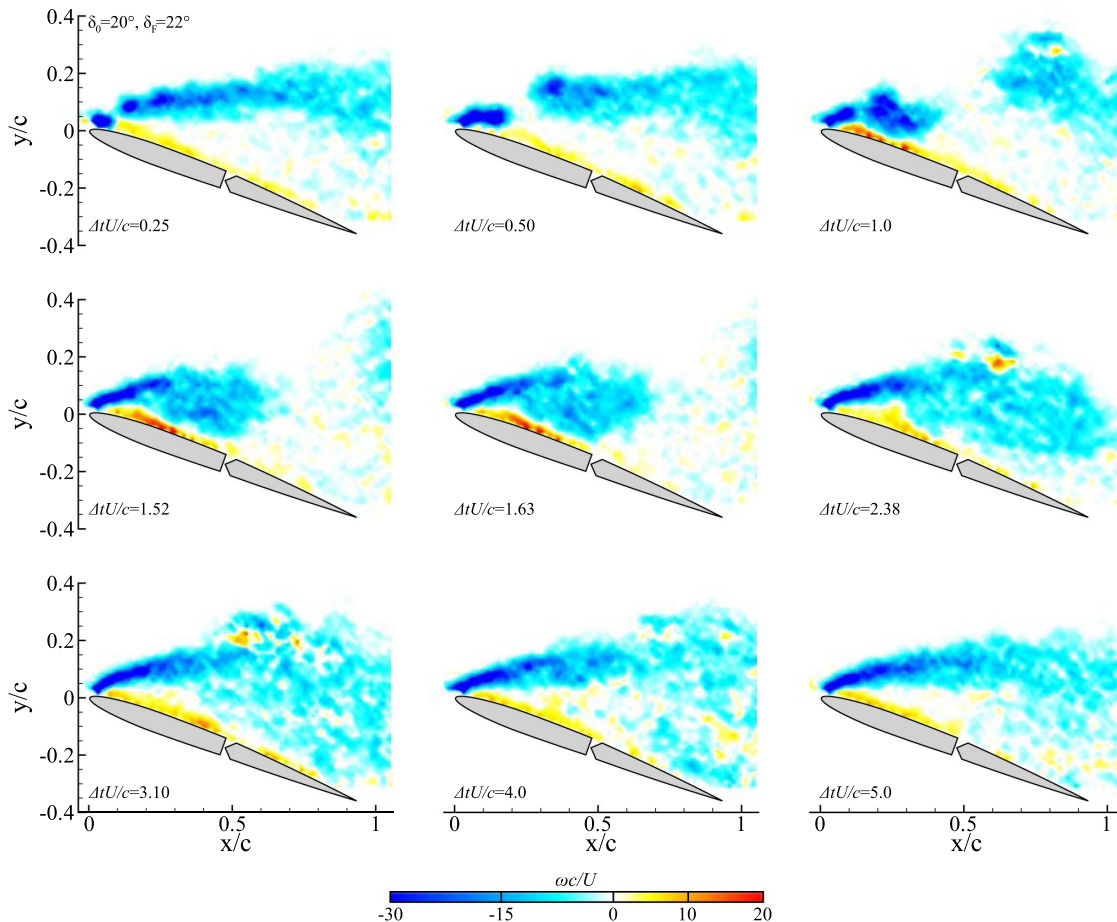


Fig. 8 Temporal evolution of vortical formations in response to a single rapid flap deflection ramp: $\Delta\delta = +2$ deg (net increase in camber) at $f = 6$ Hz.

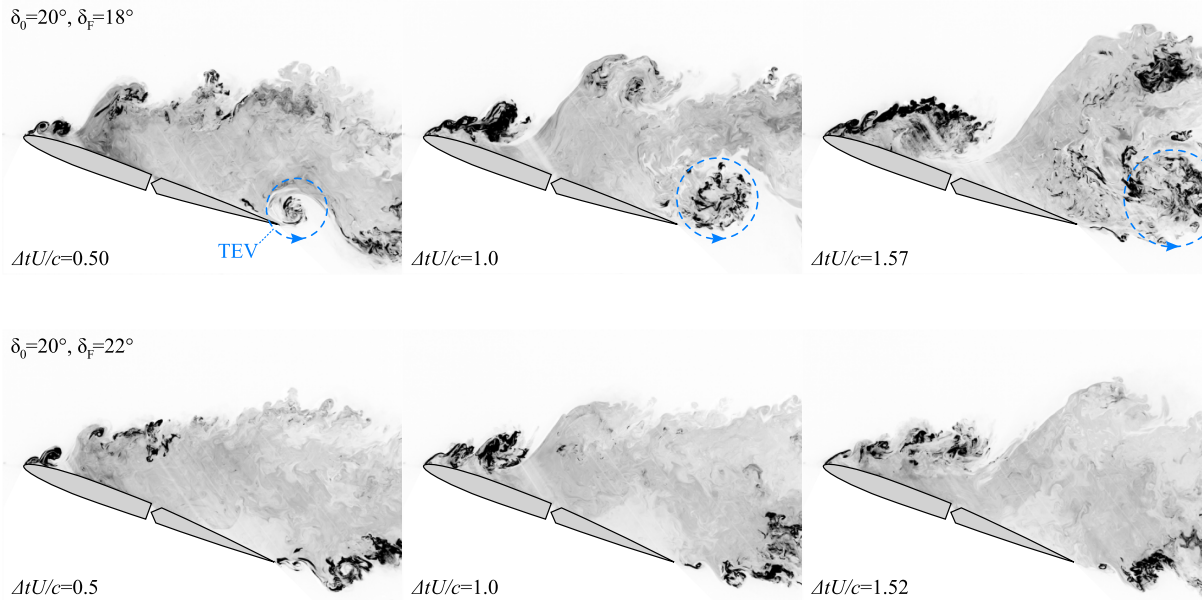


Fig. 9 Near-body wake visualization at $f = 6$ Hz. Rows: (top) $\Delta\delta = -2$ deg, (bottom) $\Delta\delta = +2$ deg.

oppositely signed vorticity. This interaction acts to neutralize the stopping vortex.

Thus far, the efficacy of rapid flap motion, independent of direction, has been demonstrated to incite disruption and rollup of the leading-edge shear layer. To better gauge the receptivity of the shear layer to the two modes of actuation, the vorticity flux is measured in Fig. 10 during the transient episode. Vorticity flux accounts only for clockwise vorticity transported across a plane oriented at $\alpha = 20$ deg and offset a distance of $0.07c$ normal from the fore-element centerline, as illustrated by the solid line in the inset image of Fig. 10. The vorticity flux is calculated by Eq. (2):

$$\dot{\Gamma}_{LE} = \int_L \omega(u_i n_i) dL \quad (2)$$

where ω is vorticity, u_i is the local velocity field, and n_i is the normal vector to the plane L . Here, the Einstein index notation is used to denote summation over repeated indices. Focus is given to the first two convective times (corresponding to the gray band of Fig. 10) encompassing the initial disruption and the coherent growth of the leading-edge vortex. As previously noted, the case of $\Delta\delta = -2$ deg prompted early separation of the incipient rollup region from the separated shear layer. To this end, we note a stark contrast in vorticity flux following the flap maneuver in Fig. 10 (left): at $\Delta tU/c \approx 1.0$,

there is a significant drop in flux for $\Delta\delta = -2$ deg, plunging toward zero; whereas the opposite is realized for $\Delta\delta = +2$ deg, where there exists a surge in flux. This plunge is congruent to the greater shear-layer disruption of $\Delta\delta = -2$ deg. In both cases, the vorticity flux returns to its baseline mean value after the transient episode is completed, approaching $\Delta tU/c = 10$, as shown by the dashed line in Fig. 10. Despite greater lift transients for the $\Delta\delta = -2$ deg case, it is the $\Delta\delta = +2$ deg case that experiences greater cumulative circulation of the leading-edge formations. Circulation here includes contributions of the shear layer and the connected leading-edge vortex. Calculation was restricted to a temporally expanding interrogation area encompassing the growth of the vortex, as shown by the dotted window in Fig. 10 (left).

D. Finite-Time Lyapunov Exponent

Although vortical flowfields serve as a good method for visualizing the differences in the wake from deflecting the flap in different directions, further insight into the complex vortex structures can be gained by using the ridges of the finite-time Lyapunov exponent (FTLE) to identify the locations of transport boundaries in the flow-field [16]. The FTLE ridges calculated in positive time are repelling material lines (pFTLEs), and FTLE ridges calculated in negative time are attracting material lines (nFTLEs). The FTLE calculations used

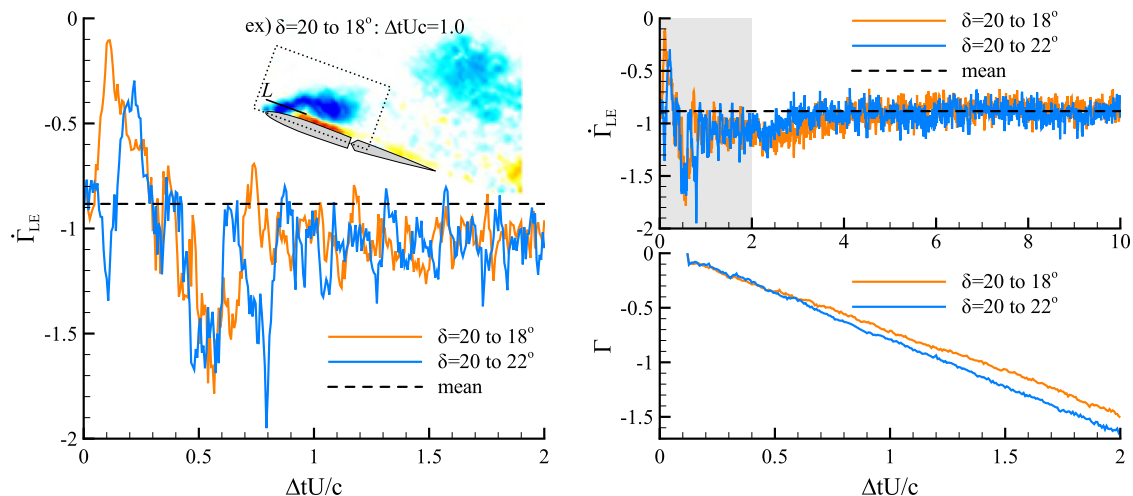


Fig. 10 Vorticity flux and leading-edge vortex circulation for $\Delta\delta = \pm 2$ deg at 6 Hz.

an integration time of $3.5tU/c$. Any particles that left the domain during particle integration were advected at the freestream velocity.

The near-wake region is visualized postactuation for both flap deflection directions using Q and the FTLE in Fig. 11. Contours of Q above $0.1Q_{\max}$ are visualized using the corresponding color bar of Fig. 11. FTLE values above 55% of the global FTLE maximum are shown in red and blue for nFTLEs and pFTLEs, respectively. The first column of images occurs at $tU/c = 0.5$, or shortly after actuation is completed, where the trailing-edge vortex is seen in the $\Delta\delta = -2$ deg case but is not visible in the $\Delta\delta = +2$ deg case. The separated shear layer contains a larger vortex for $\Delta\delta = -2$ deg than for $\Delta\delta = +2$ deg, but the shear layers exhibit similar structure otherwise. Both images show the initial formation of a leading-edge vortex (LEV) of similar size. The second column occurs when the leading-edge vortex is forming at $tU/c = 1.0$. The separated shear layers have both rolled up into a similarly sized and located vortex, with the previously observed larger vortex for $\Delta\delta = -2$ deg now showing no difference from $\Delta\delta = +2$ deg. The observed single large leading-edge vortex found in the flow visualization for $\Delta\delta = -2$ deg is also seen in the corresponding FTLE (Fig. 11); and the $\Delta\delta = +2$ deg results agree with the flow visualization and show two distinct structures in the leading-edge vortex, which are separated by nFTLE ridges in Fig. 11. The third column shows the FTLE field at $tU/c = 1.5$, where the leading-edge vortex has grown in size to cover more than half of the airfoil suction surface. The two smaller vortices present at $tU/c = 1.0$ in $\Delta\delta = +2$ deg have now combined into one LEV, resulting in a similar leading-edge vortex structure for both directions of flap movement.

The shape of the outermost pFTLE ridge that delineates the recirculating region of trapped fluid near the airfoil from the surrounding flow is different between the two cases, and its movement showcases the differences in entrainment near the trailing edge. For the $\Delta\delta = -2$ deg case, the blue pFTLE ridge near the trailing edge nearly touches the suction surface of the airfoil (green arrow) just upstream of the trailing-edge vortex at $tU/c = 0.5$ (Fig. 11). This trailing-edge vortex is rotating counterclockwise, and therefore entraining fluid down toward the suction surface of the airfoil on the upstream side of the vortex. This causes the nearby pFTLE ridge to move toward to the

airfoil surface over time. At later times ($tU/c = 1.0$), the trailing-edge vortex has begun to convect downstream away from the airfoil, but the fluid entrained by the vortex is still keeping the outermost pFTLE ridge close to the airfoil surface. Once the trailing-edge vortex has convected sufficiently far away from the trailing edge to have a diminished effect, the flow induced by the leading-edge vortex begins to dominate. This leads to reattachment near the trailing edge at $tU/c = 1.5$ for $\Delta\delta = -2$ deg and, at later times, causes the outermost pFTLE ridge to begin moving away from the airfoil surface as the leading-edge vortex approaches the trailing edge.

The same pFTLE ridge displays significantly different behavior for the $\Delta\delta = +2$ deg case. This motion does not generate a clear trailing-edge vortex, and therefore the induced velocity toward the airfoil suction surface near the trailing edge does not exist. As a consequence, the outermost pFTLE ridge at $tU/c = 0.5$ in Fig. 11 is significantly farther away from the airfoil surface near the trailing edge than in $\Delta\delta = -2$ deg. As the flowfield evolves in time, this pFTLE ridge continues to advect away from the airfoil surface, resulting in a larger region of recirculating flow above the airfoil at $tU/c = 1.0$ for $\Delta\delta = +2$ deg as compared with -2 deg. The lack of entrainment near the trailing edge for the $\Delta\delta = +2$ deg motion also results in the flow never reattaching. The large recirculation region caused by this continued flow separation results in the lower postmotion peak lift value at $tU/c = 2.7$ as compared to the $\Delta\delta = -2$ deg case. Overall, the FTLE results corroborate the conclusions drawn from dye visualization while adding additional information on entrainment and reattachment in the trailing-edge region.

E. Modal Decomposition

Despite markedly similar flowfield responses garnered among the two actuation cases (albeit with potential temporal offsets), the temporal force histories are distinct. Here, the proper orthogonal decomposition (POD) is performed to help elucidate these distinctive force outputs [17,18] by reducing the evolution of the vorticity field $\omega(x, y, z, t)$ to an approximate representation in terms of a small number of linearly uncorrelated POD modes $\phi_j(x, y, z)$ [17]:

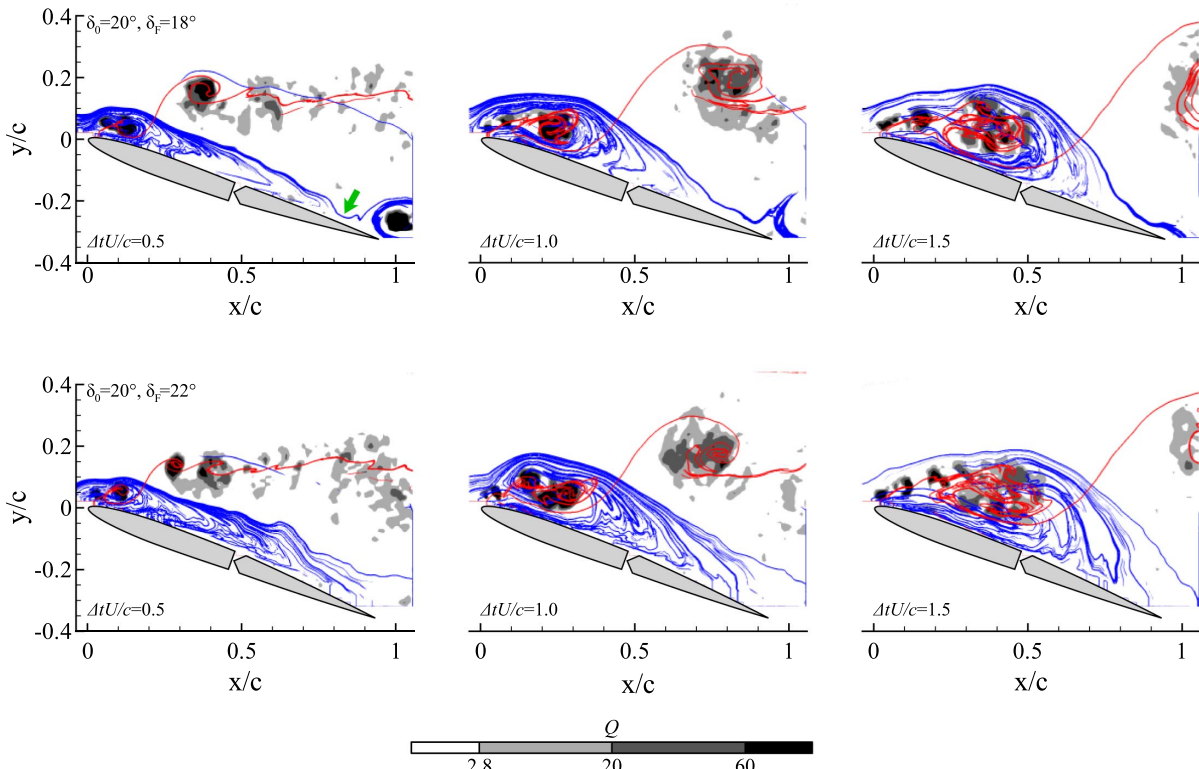


Fig. 11 Wake visualization Q criterion (gray contours), nFTLE ridges (red), and pFTLE ridges (blue) at $f = 6$ Hz. Rows: (top) $\Delta\delta = -2$ deg, (bottom) $\Delta\delta = +2$ deg.

$$\omega(x, y, z, t) = \bar{\omega}(x, y, z, t) + \sum_j a_j(t) \phi_j(x, y, z) \quad (3)$$

where $\bar{\omega}$ denotes the evolution of the baseline vorticity field, and a_j denotes the coefficient associated with the j th POD mode ϕ_j . The POD modes ϕ_j can be computed by means of the snapshot POD method [19], which decomposes a matrix of snapshot data into spatial eigenmodes and temporal coefficients on an energy basis. Here, the computation is performed using the singular value decomposition of a matrix for which the columns $\Delta\omega_i$ are snapshots of the baseline subtracted vorticity, i.e., $\Delta\omega_i = \omega(x, y, z, t_i) - \bar{\omega}(x, y, z, t_i)$. If the number of linearly independent snapshots m is less than the size of each snapshot n , then this is simply

$$[\Delta\omega_1 \ \Delta\omega_2 \ \cdots \ \Delta\omega_m] = [\phi_1 \ \phi_2 \ \cdots \ \phi_m] \Sigma \Psi^T \quad (4)$$

Here, $\Sigma = \text{diag}(\sigma_1, \dots, \sigma_m)$ is sorted such that σ_j are nonincreasing, revealing the relative significance of each mode in an energy sense.

The results are presented in Fig. 12. The analysis here is limited to the six most energetic modes. A total of 1557 snapshots was included in the analysis, amounting to 10.38 convective times of time-resolved PIV. The series of snapshots corresponds to the entire transient episode following flap actuation and concluding at the nominal relaxation of the flow to a baseline state.

The cumulative mode energy is presented in Fig. 13, where the first six modes account for 55 and 61% of the total energy for $\Delta\delta = +2$ deg and -2 deg cases, respectively. The most energetic mode of the two cases (mode 1) is highly representative of free-shear-layer disruption by incipient rollup. Indeed, the corresponding temporal coefficient among both cases is marked by a singular peak that rises during vortex formation and gradually relaxes in time, as shown in Fig. 14. The subsequent modes of Fig. 12 showcase prominent high-curvature vorticity contours clustered toward the leading edge. These modes are maximal during the initial transitory stages of leading-edge vortex production. Despite overwhelming modal agreement between the two ramp cases, it is noted that temporal

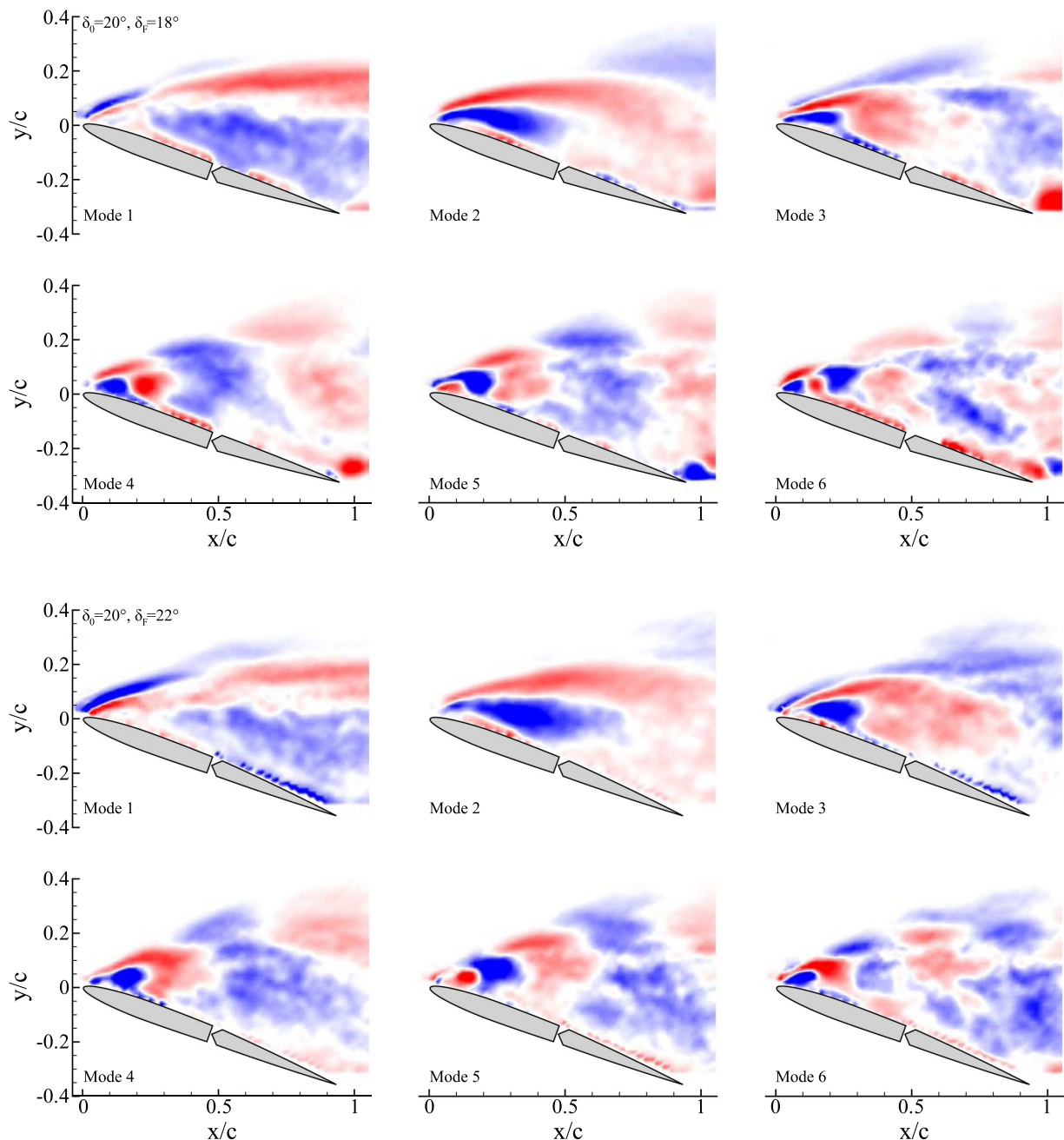


Fig. 12 POD modes 1-6 for $f = 6$ Hz: (top) $\Delta\delta = -2$ deg, (bottom) $\Delta\delta = +2$ deg.

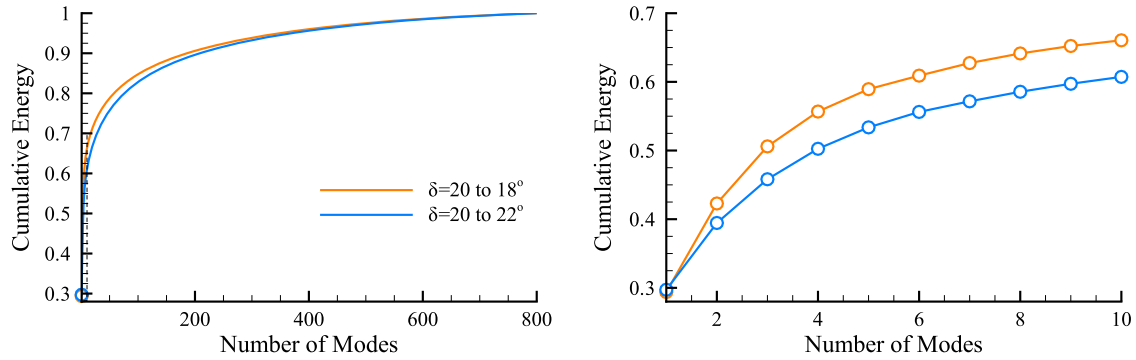


Fig. 13 Cumulative energy of POD modes.

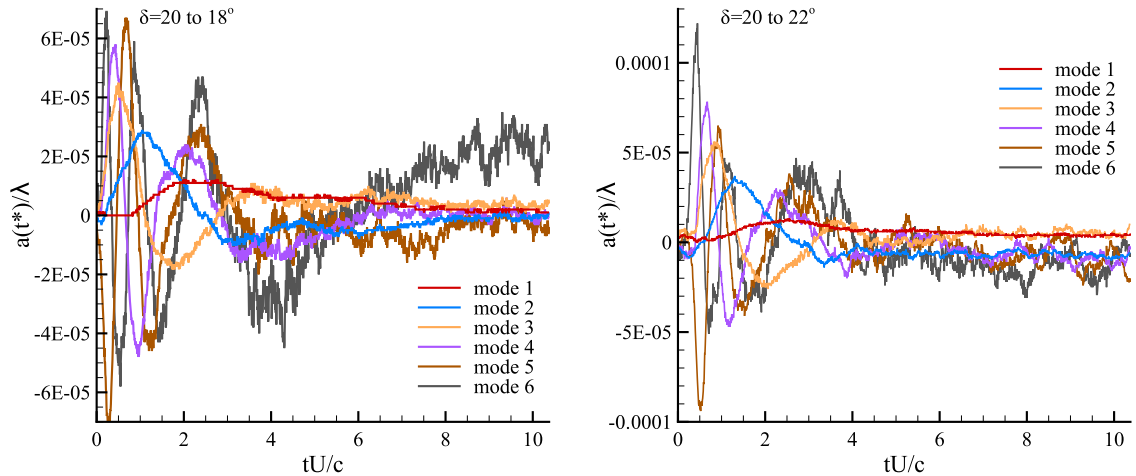


Fig. 14 Temporal coefficient values for POD modes of Fig. 12: (left) $\Delta\delta = -2$ deg (right) $\Delta\delta = +2$ deg.

coefficients of modes 2 and 3 for $\Delta\delta = +2$ deg bear a minor delay peak from that observed for $\Delta\delta = -2$ deg. This observation, coupled with the vorticity fields of Fig. 7, supports the narrative of enhanced disruption of the shear layer through retardation of vorticity flux to hasten the formation of a coherent leading-edge vortex.

IV. Conclusions

The transient effects of low-amplitude high-rate flap deflection on the lift and drag forces of a massively separated NACA 0006 airfoil were investigated. The airfoil flap was driven to perform a step in deflection angle within a fraction of one convective time. It was found that the ensuing force histories were highly dependent on the direction of flap actuation. In the case of $\Delta\delta = -2$ deg, which amounts to a negative camber, the transient lift response bore the hallmarks of conventional fluidic actuators: an initial antilift spike, followed by lift recovery and then a surge in lift to a global maximum, and then a gradual relaxation to resume steady-state performance. In reversing the flap direction to $\Delta\delta = +2$ deg, the transient force response was devoid of the deleterious antilift spike but instead produced an immediate incremented lift exceeding steady-state performance. Regardless of ramp direction, it appeared that the duration of force transients remained unaffected and scaled with convective time. A survey of ramp-rate effects revealed that a negative-camber motion ($\Delta\delta = -2$ deg) bore a greater response in transient lift amplitude. Conversely, there appeared to be less dependency on ramp rate for positive-camber transients ($\Delta\delta = +2$ deg) up until a hypothesized threshold of bound circulation. Given the instantaneous response of the lift to rapid flap deflection, the flap was considered to be performing with an inviscid efficiency. Although both flap deflection cases proved disruptive to the leading-edge free-shear layer, it was the $\Delta\delta = -2$ deg case that prompted a significant reduction in vorticity flux feeding the free-shear layer. Through FTLEs, it was revealed that the negative-camber motion ($\Delta\delta = -2$ deg) provided for significant

entrainment near the trailing-edge. The pFTLE ridges had a reduced distance from the suction surface when compared to those of positive-camber motion ($\Delta\delta = +2$ deg). This proximity is understood to correlate with the elevated lift transient peak achieved in the $\Delta\delta = -2$ deg case. Through modal analysis, it was revealed that the POD modes and temporal coefficient profiles were markedly similar between the two cases. However, the $\Delta\delta = +2$ deg motion was met with temporal lag among the coefficient peaks. This is believed to be a product of the greater disruption incurred in $\Delta\delta = -2$ deg deflection where the formation of a coherent leading-edge vortex was initially hastened.

Acknowledgments

M. S. Hemati acknowledges support from the Air Force Office of Scientific Research (AFOSR) Grant No. FA9550-17-1-0252 and FA9550-19-1-0034. This work is motivated by objectives outlined by members of the *AIAA FDTC Massively-Separated Flows Discussion Group* including investigation of flow control opportunities in low Reynolds number flows for unsteady load mitigation.

References

- [1] Williams, D. R., Kerstens, W., Pfeiffer, J., King, R., and Colonius, T., "Unsteady Lift Suppression with a Robust Closed Loop Controller," *Active Flow Control II*, edited by R. King, Vol. 108, Springer-Verlag, Heidelberg, Germany, 2010, pp. 19–30.
- [2] Raju, R., Mittal, R., and Cattafesta, L., "Dynamics of Airfoil Separation Control Using Zero-Net-Mass-Flux Forcing," *AIAA Journal*, Vol. 46, No. 12, 2008, pp. 3103–3115. <https://doi.org/10.2514/1.37147>
- [3] Albrecht, T., Weier, T., Gerbeth, G., Monnier, B., and Williams, D. R., "Separated Flow Response to Single Pulse Actuation," *AIAA Journal*, Vol. 53, No. 1, 2015, pp. 190–199. <https://doi.org/10.2514/1.J053026>

- [4] Brzozowski, D. P., Woo, G. T. K., Culp, J. R., and Glezer, A., "Transient Separation Control Using Pulse-Combustion Actuation," *AIAA Journal*, Vol. 48, No. 11, 2010, pp. 2482–2490.
<https://doi.org/10.2514/1.45904>
- [5] Amitay, M., and Glezer, A., "Role of Actuation Frequency in Controlled Flow Reattachment over a Stalled Airfoil," *AIAA Journal*, Vol. 40, No. 2, 2002, pp. 209–216.
<https://doi.org/10.2514/2.1662>
- [6] Amitay, M., and Glezer, A., "Flow Transients Induced on a 2D Airfoil by Pulse-Modulated Actuation," *Experiments in Fluids*, Vol. 40, No. 2, 2006, pp. 329–331.
<https://doi.org/10.1007/s00348-005-0069-6>
- [7] Margalit, S., Greenblatt, D., Seifert, A., and Wynanski, I., "Delta Wing Stall and Roll Control Using Segmented Piezoelectric Fluid Actuators," *Journal of Aircraft*, Vol. 42, No. 3, 2005, pp. 698–709.
<https://doi.org/10.2514/1.6904>
- [8] Natarajan, M., Freund, J. B., and Bodony, D. J., "Actuator Selection and Placement for Localized Feedback Flow Control," *Journal of Fluid Mechanics*, Vol. 809, Dec. 2016, pp. 775–792.
<https://doi.org/10.1017/jfm.2016.700>
- [9] Chomaz, J. M., "Global Instabilities in Spatially Developing in Flows: Non-Normality and Nonlinearity," *Annual Review of Fluid Mechanics*, Vol. 37, No. 1, 2005, pp. 357–392.
<https://doi.org/10.1146/annurev.fluid.37.061903.175810>
- [10] Huang, L., Huang, P. G., and LeBeau, R. P., "Numerical Study of Blowing and Suction Control Mechanism on NACA0012 Airfoil," *Journal of Aircraft*, Vol. 41, No. 5, 2004, pp. 1005–1013.
<https://doi.org/10.2514/1.2255>
- [11] Granlund, K., Monnier, B., Ol, M. V., and Williams, D., "Airfoil Longitudinal Gust Response in Separated vs Attached Flows," *Physics of Fluids*, Vol. 26, No. 2, 2014, Paper 027103.
<https://doi.org/10.1063/1.4864338>
- [12] Ol, M. V., Eldredge, J. D., and Wang, C., "High-Amplitude Pitch of a Flat Plate: An Abstraction of Perching and Flapping," *International Journal of Micro Air Vehicles*, Vol. 1, No. 3, 2009, pp. 203–216.
<https://doi.org/10.1260/175682909789996186>
- [13] Granlund, K. O., Ol, M. V., and Bernal, L. P., "Unsteady Pitching Flat Plates," *Journal of Fluid Mechanics*, Vol. 733, Oct. 2013, Paper R5.
<https://doi.org/10.1017/jfm.2013.444>
- [14] Medina, A., Ol, M. V., Williams, D., An, X., and Hemati, M., "Modeling of Conventional Flaps at High Deflection-Rate," *55th AIAA Aerospace Sciences Meeting, AIAA SciTech Forum*, AIAA Paper 2017-1230, 2017.
<https://doi.org/10.2514/6.2017-1230>
- [15] Medina, A., Ol, M. V., Mancini, P., and Jones, A. R., "Revisiting Conventional Flaps at High Deflection Rate," *AIAA Journal*, Vol. 55, No. 8, 2017, pp. 2676–2685.
<https://doi.org/10.2514/1.J055754>
- [16] Haller, G., "Distinguished Material Surfaces and Coherent Structures in Three-Dimensional Fluid Flows," *Physica D*, Vol. 149, No. 4, 2001, pp. 248–277.
[https://doi.org/10.1016/S0167-2789\(00\)00199-8](https://doi.org/10.1016/S0167-2789(00)00199-8)
- [17] Holmes, P., Lumley, J., Berkooz, G., and Rowley, C., "Proper Orthogonal Decomposition," *Turbulence, Coherent Structures, Dynamical Systems and Symmetry*, 2nd ed., Cambridge Univ. Press, Cambridge, 2012, pp. 68–105.
<https://doi.org/10.1017/CBO9780511919701.005>
- [18] Taira, K., Brunton, S. L., Rowley, C. W., Colonius, T., McKeon, B. J., Schmidt, O. T., Gordeyev, S., Theofilis, V., and Ukeiley, L. S., "Modal Analysis of Fluid Flows: An Overview," *AIAA Journal*, Vol. 55, No. 12, 2017, pp. 4013–4041.
<https://doi.org/10.2514/1.J056060>
- [19] Sirovich, L., "Turbulence and the Dynamics of Coherent Structures Part I-III," *Quarterly of Applied Mathematics*, Vol. 45, No. 3, 1987, pp. 561–571.
<https://doi.org/10.1090/qam/1987-45-03>

H. Dong
 Associate Editor